



Performance Analysis and Limiting Parameters of Cross-flow Membrane-based Liquid-desiccant Air Dehumidifiers

Behnam Ahmadi ^a, Masoud Ahmadi ^a, Kashif Nawaz ^b, Ayyoub M. Momen ^b, Sajjad Bigham ^{a,*}

^a Department of Mechanical Engineering-Engineering Mechanics, Michigan Technological University, 1400 Townsend Drive, Houghton, MI 49931-1295, USA

^b Building Technologies Research and Integration Center, Oak Ridge National Laboratory, One Bethel Valley Road, P.O. Box 2008, MS-6070, Oak Ridge, TN 37831-6070, USA

ARTICLE INFO

Article history:

Received 20 April 2021

Received in revised form 21 August 2021

Accepted 9 September 2021

Keywords:

Air conditioning systems

Air dehumidifier

Liquid-desiccant-based systems

Porous superhydrophobic membrane

Separate sensible and latent cooling concept

Two-phase, multi-species CFD simulations

ABSTRACT

To dehumidify a humid air stream, existing air conditioning (AC) systems substantially overcool the outdoor humid air below its dew point, thereby significantly reducing energy efficiency. Directly capturing humidity, membrane-based liquid-desiccant dehumidification systems separate sensible and latent cooling (SSLC) loads and thus offer a promising pathway for a high-performance AC solution. Design of an energy-efficient SSLC-AC system, however, rests largely on detailed understating of the dehumidification process. While some studies have identified the dehumidification process mainly depends on membrane characteristics, other studies have argued that the process is limited by desiccant liquid or alternatively air thermo-hydraulic physics for typical humid climate conditions. The present study examines performance and physics of the membrane-based liquid-desiccant dehumidification process over a wide range of climate conditions through a novel 3D, two-phase, multi-species CFD model. Decoupling the thermodynamic and hydraulic effects, the study reveals that the dehumidification rate is a linear function of the water vapor pressure potential ($J = \alpha \Delta P$) summarizing the system's thermodynamic state. The slope of the curve (i.e., α) depends on hydraulic transport characteristics of the membrane pores, air stream, and desiccant solution. More importantly, it was found that the air dehumidification process is mainly limited by the air-side transport physics for thin liquid-desiccant films and commonly used porous superhydrophobic membranes. Additionally, results show that, depending on ambient/desiccant conditions and physical dehumidifier characteristics, energy effectiveness and dehumidification rate vary from 13 to 34% and from 0.13 to 1.4 $\text{g m}^{-2} \text{s}^{-1}$, respectively. Therefore, the present study allows to efficiently design future SSLC-based AC systems exhibiting high performance energy metrics.

© 2021

Nomenclatures

Acronyms

2D Two-dimensional

3D	Three-dimensional
AC	Air conditioning
CFD	Computational fluid dynamic
DCHX	Desiccant coated heat exchanger
DEVap	Desiccant enhanced evaporative air conditioning
LD	Liquid-desiccant
SD	Solid desiccant
SSLC	Separate sensible and latent cooling
UDF	User defined function

Greek letters

α	Thermal diffusivity
η	Effectiveness
ρ	Density
κ_m	Membrane permeability
δ_m	Membrane thickness

* This manuscript has been authored by UT-Battelle, LLC, under contract DE-AC05-00OR22725 with the US Department of Energy (DOE). The US government retains and the publisher, by accepting the article for publication, acknowledges that the US government retains a nonexclusive, paid-up, irrevocable, worldwide license to publish or reproduce the published form of this manuscript, or allow others to do so, for US government purposes. DOE will provide public access to these results of federally sponsored research in accordance with the DOE Public Access Plan (<http://energy.gov/downloads/doe-public-access-plan>).

* Corresponding author.

E-mail address: sbigham@mtu.edu (S. Bigham).

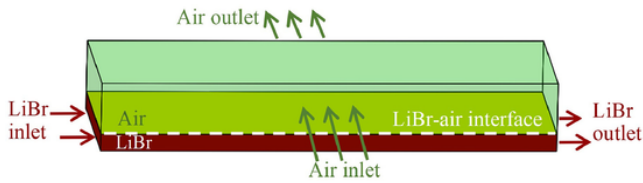


Fig. 1. A schematic of the dehumidifier model.

In	Inlet
Out	Outlet
M	Membrane
S	Solution

1. Introduction

The world AC demand is estimated to triple from 1.6 billion units today to 5.6 billion units in 2050; accounting for 10 new ACs sold every second for the next 30 years (IEA, 2018). The rise in the AC market is mainly due to population growth and increasing urbanization, particularly in the emerging world. Considering energy rating of existing AC systems, the additional electricity needed to power the rising AC demand is as much as the current use of the US, the EU, and Japan combined, thereby creating one of the most crucial blind spots in today's energy policy. Therefore, development of new high-performance AC systems is of utmost importance to avoid facing an energy “cold crunch” (IEA, 2018).

Most widely used AC systems today utilize a century-old technology invented by Willis Carrier and energy-hungry mechanical vapor compressors to create the cooling effect through a direct expansion refrigeration cycle. These standard AC systems cannot efficiently decouple the sensible (i.e., temperature) and latent (i.e., humidity) cooling loads. Therefore, they substantially overcool an outdoor humid air to below its dew point temperature, reducing absolute humidity and thus dehumidifying the air stream. As the air stream gets highly saturated (i.e., high relative humidity) at lower temperatures particularly in the vicinity of the dew point temperature, it is then often heated to decrease its relative humidity and return back to the comfort zone (Bai et al., 2017; Shen et al., 2016). Both air overcooling and subsequent heating processes significantly degrade energy efficiency of current AC systems.

A large portion of the AC energy usage can be potentially saved if separate sensible and latent cooling (SSLC) systems in which latent cooling load is isolated and treated by a distinct desiccant unit are employed. Prior studies have identified that the SSLC systems could reduce the AC energy consumption by 30–90% depending on latent cooling load levels (Kozubal et al., 2011; Lee et al., 2016; Ling et al., 2013). Existing desiccant-based dehumidification methods can be classified as (i) solid-desiccant (SD) wheel/coated surfaces (Narayanan et al., 2013; Comino et al., 2020; Tu et al., 2018; Higashi et al., 2018; Restuccia et al., 2005; O'Connor et al., 2016; Zhou et al., 2018; Pandelidis et al., 2020; Tu et al., 2014; Goldsworthy and White, 2012; Cabeza et al., 2017; Bahremand and Bahrani, 2019), (ii) falling-film/spray/wick liquid-desiccant systems (Mortazavi et al., 2015; Cheng et al., 2020; Cho et al., 2019; Wen and Lu, 2019), and (iii) membrane-based liquid-desiccant systems (S Bigham et al., 2014; Nasr Isfahani et al., 2014; S Bigham et al., 2014; Lin et al., 2019; Asfand and Bourouis, 2015; Chu et al., 2019; Huang et al., 2018; Bai et al., 2020; Das and Jain, 2015). Performance of desiccant-based dehumidifiers, however, is highly sensitive to their architectural designs and thermohydraulic operating conditions of both air and desiccant materials selected. If designed poorly, these dehumidifiers could suffer from a low moisture absorption rate leading to systems that are bulkier, costlier, and less energy efficient. Therefore, a detailed understanding of the nature of moisture removal process is critical to an accurate design and efficient operation of the desiccant-based dehumidifiers.

Solid-desiccant drying wheels are one of the most commonly used desiccant dehumidification systems. A desiccant wheel consists of a honeycomb structure coated with or entirely fabricated from a solid desiccant medium. The wheel slowly rotating at a rate of 10 to 30 rotations per hour absorbs moisture from a humid outdoor air stream and desorbs it to a hot regeneration air stream. A major research focus on desiccant wheel systems has been to improve the solid-desiccant dehu-

Table 1

Nominal input parameters of the numerical model.

Parameter	Value [unit]
Inlet LiBr solution temperature, $T_{sol,in}$	30 °C
Inlet LiBr solution concentration, C_{in}	55%
Inlet LiBr solution velocity, $V_{sol,in}$	0.03 m s ⁻¹
Inlet air temperature, $T_{air,in}$	35 °C
Inlet air relative humidity, Φ_{in}	80%
Inlet air velocity, $V_{air,in}$	4 m s ⁻¹
LiBr solution channel thickness, D_{sol}	200 μm
Air channel thickness, D_{air}	3 mm
LiBr solution channel length, L	0.127 m
LiBr solution channel width, W	0.051 m
Membrane porosity, ϵ	60%
Membrane pore diameter, d_m	1 μm
Tortuosity, τ	1.0
Membrane thickness, δ_m	20 μm
Membrane permeability, κ_m	3.25×10^{-4} s m ⁻¹

τ	Membrane tortuosity
μ	Dynamic viscosity
ω	Air humidity ratio
ϵ	Porosity
δ	Solution film thickness
Φ	Air relative humidity

Chemical symbols

LiBr	Lithium Bromide
$H_2O(v)$	Water vapor
$H_2O(l)$	Liquid water

Symbols

v	Velocity
T	Temperature
C	Liquid-desiccant concentration
p	Pressure
J	Water vapor mass flux
h_{fg}	Latent heat of vaporization
H	Enthalpy
K	Thermal conductivity
M	Molecular weight
R	Membrane pore size
P_v	Water vapor partial pressure of the air
$P_{s,w}$	Water vapor pressure at the desiccant-air interface
R	Gas constant
d_m	Membrane pore diameter
D	Channel thickness
L	Channel length
W	Channel width

Subscripts

Int.	Interface
------	-----------

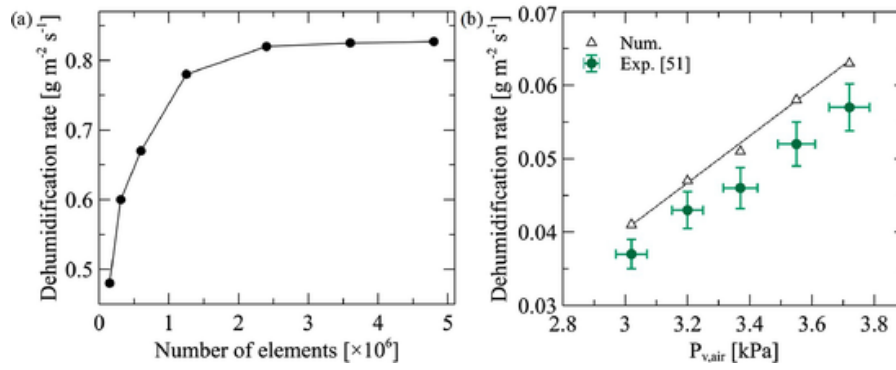


Fig. 2. (a) Dehumidification rate at different numbers of computational elements, and (b) validation of the numerical model against experimental data.

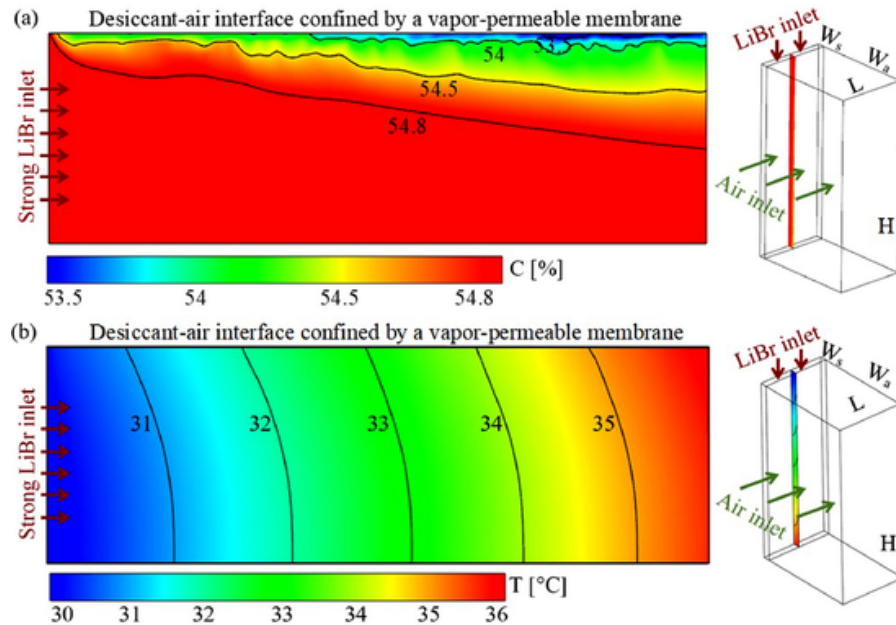


Fig. 3. (a) LiBr solution, and (b) temperature distribution contours within the desiccant flow channel.

midification capacity through an isothermal adsorption process accomplished by either an internally cooled dehumidifier (Narayanan et al., 2013; Zhou et al., 2018) or multi-stage rotary disks (Tu et al., 2014; Ge et al., 2009). A desiccant coated heat exchanger (DCHX) is an alternative configuration allowing a near isothermal adsorption process through simultaneous dehumidification and desiccant cooling. Here, the thermal contact between heat exchanger surfaces and desiccant media is maximized, thereby leading to high heat and mass transfer rates (Restuccia et al., 2005). Attempts have been also made to decrease required regeneration temperature and pressure drop across the wheel (Tu et al., 2018; O'Connor et al., 2016). Solid-desiccant systems, however, demonstrate low dehumidification capacities often aggravated by high regeneration temperatures (Misha et al., 2012).

Liquid-desiccant-based dehumidifiers, on the other hand, offer higher moisture removal rates and energy efficiencies compared to their solid counterparts (Misha et al., 2012). While the humidity could be only adsorbed on the outer surface of a solid-desiccant medium, the whole volume of a liquid-desiccant solution is involved in the moisture absorption process leading to high dehumidification rates. The typical architectural design of a liquid desiccant-based dehumidifier is a falling-film absorber. A study conducted by Islam et al. (Raisul Islam et al., 2003) showed that a falling-film inverting absorbers with alternatively cooled surfaces could increase vapor absorption rate by 100% compared to a tubular design. Falling film dehumidifiers of liquid-desiccant solutions over textured surfaces have also shown promises on

enhanced moisture removal rates (Mortazavi et al., 2015; Tao et al., 2019). Falling film dehumidifiers, however, exhibit liquid desiccant droplet carryover into a supply air stream, potentially introducing health risks to building occupants and corrosion to metal ducts.

Membrane-based liquid-desiccant (LD) dehumidifiers introduce a porous barrier layer between the LD and air streams, thereby suppressing desiccant entrainment into the air (Liu et al., 2019; Ren et al., 2019). Here, the LD solution is constrained by a vapor-permeable membrane allowing the moisture absorption process at the liquid menisci formed at the desiccant-air membrane interface. Several prior studies have experimentally and numerically investigated membrane-based liquid-desiccant dehumidifier systems. A major focus of experimental efforts has been to examine moisture removal potential and overall system performance (Mortazavi et al., 2015; Luo et al., 2017; Park et al., 2019; Su et al., 2018). The desiccant enhanced evaporative air conditioner (DEVap) concept (Kozubal et al., 2011), for instance, employed membrane technology to contain both the liquid desiccant and water solutions. This allowed to efficiently cool the liquid desiccant by an indirect evaporative cooling, thereby leading to an enhanced dehumidification process. Although greatly valuable in understanding the overall dehumidifier performance, experimental results are largely unable to reveal the underlying mechanisms of the dehumidification process.

Details of the membrane-based liquid-desiccant dehumidification process could be better revealed by computational fluid dynamic (CFD) simulations (Lin et al., 2019; Das and Jain, 2015; Jafarian et al., 2019;

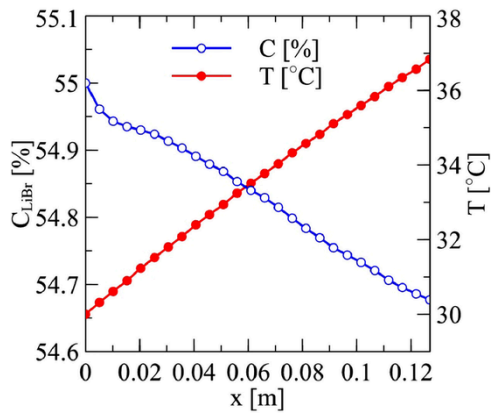


Fig. 4. Variations of the average LiBr concentration and temperature along the desiccant flow channel.

Rashidzadeh et al., 2019; SM Huang et al., 2012; Huang et al., 2014; Huang et al., 2013; Zhang, 2011; Zhang et al., 2012; S-M Huang et al., 2012; Afrasiabian et al., 2019). Das and Jain (Das and Jain, 2015) developed a 2D steady-state mathematical model to study performance of the membrane contactors for liquid desiccant systems. They investigated variations of key parameters including enthalpy, humidity and concentration fields within the membrane contactor. More importantly, it was argued that performance of the contactor mainly depends on the membrane characteristics, mainly porosity, pore size and thickness. Woods and Kozubal (Woods and Kozubal, 2018) utilized a finite-difference model to investigate an internally-cooled, 3-fluid membrane contactor for the liquid-desiccant-based air dehumidification process. In contrast to the previous study identifying membrane as the limiting step, they concluded that the dehumidification process is dominated by the air-side heat and mass transfer resistances. Interestingly, the membrane and cooling water heat transfer resistances were found to be the least important. Lin et al. (Lin et al., 2019) recently performed a scaling and dimensional analysis of a cross-flow membrane liquid desiccant dehumidifier through 2D CFD simulations. They identified relevant dimensionless numbers that dictate performance of a membrane-based liquid desiccant dehumidifier. They argued that the heat and mass convection, heat conduction, and mass diffusion of both air and solution sides are the dominating factors.

Evidently, despite remarkable progress in examining nature of the membrane-based liquid-desiccant dehumidification process, the existing literature suggests mixed conclusions on the dominant sub-mechanism process. Particularly, existing simulation models do not reveal complex thermo-hydraulic transport effects including 3D moisture boundary layer growth and interfacial concentration/temperature distributions to address this knowledge gap. The present work utilizes novel 3-dimensional (3D), two-phase, multi-species CFD simulations to better understand physics of water extraction process from humid ambient air at a broad range of working conditions. Decoupling the roles of thermodynamic and hydraulic parameters in the dehumidification process, the study clearly identifies the rate-limiting sub-mechanism in the membrane-based liquid-desiccant dehumidification process. In the following sections, first, the numerical model including assumptions, governing equations, and boundary conditions are discussed in details. Then, the model accuracy and grid independency are studied. Finally, physics, moisture removal rate, and energy effectiveness of the membrane-based LD dehumidification process at different air and desiccant thermo-hydraulic operating conditions and physical dehumidifier characteristics are examined.

2. Numerical model

Detailed 3D, two-phase (i.e., liquid and gas phases), multi-species CFD simulations were conducted to analyze performance of a membrane-based dehumidifier module. The two phases are separated by a porous superhydrophobic membrane. The following assumptions are made to perform the numerical modeling.

- 1 All involved heat and mass transfer processes are assumed to be steady-state.
- 2 The liquid-desiccant and air flow streams are considered to be laminar.
- 3 The liquid phase consists of the desiccant and liquid water species.
- 4 The gas phase is comprised of air and water vapor molecules.
- 5 As the focus of the current study is to examine mass transport in a thin desiccant solution film constrained by a membrane, the gravity effect is neglected.
- 6 The liquid and gas phases are in a thermodynamic equilibrium state at the desiccant-air interface.
- 7 The mass diffusion process across the membrane is steady-state without any storage.

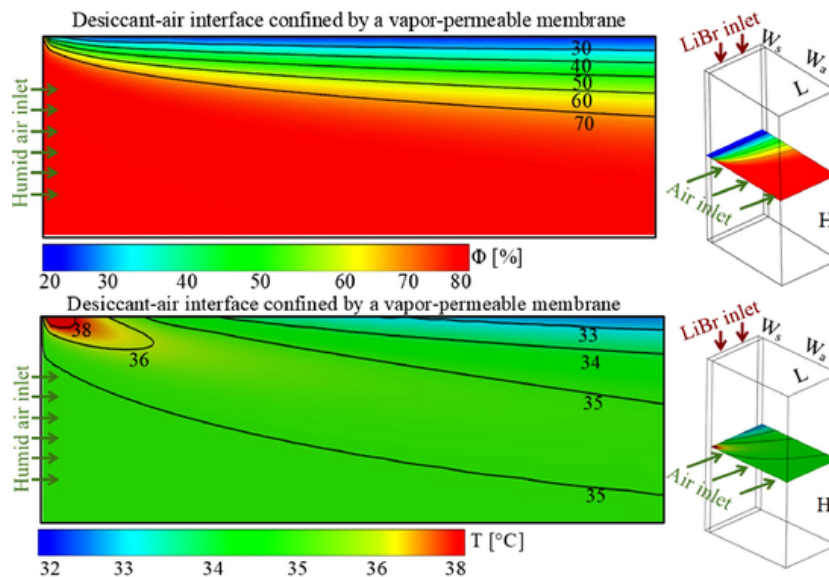


Fig. 5. (a) Air relative humidity and (b) temperature distribution contours within the air flow channel.

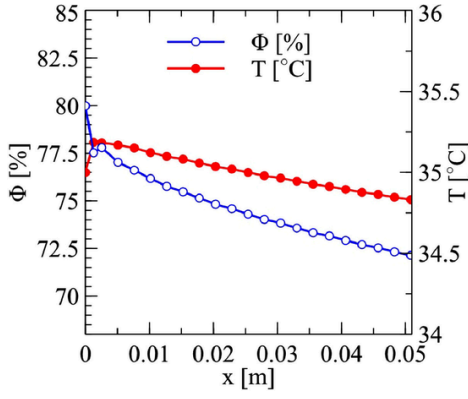


Fig. 6. Variations of the average air relative humidity and temperature along the air flow channel.

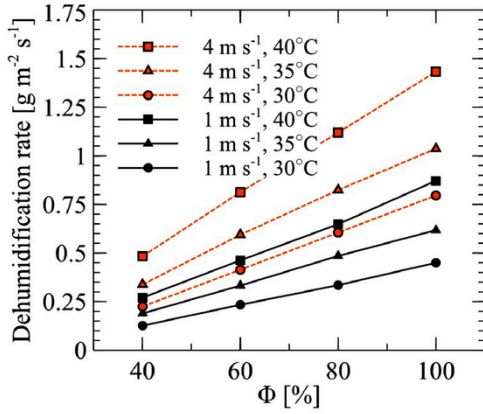


Fig. 7. Variations of moisture removal rate versus relative humidity at different air inlet temperatures and velocities.

8 The membrane in-plane permeability is negligible compared with the membrane through-plane permeability. Therefore, a one-dimensional water vapor mass transport through the membrane is considered.

The numerical procedure consists of two steps. In the first step, a continuum-based approach was used to model heat and mass transport processes inside the desiccant solution (i.e., liquid phase) and air domain (i.e., gas phase). The momentum, energy, liquid-desiccant, and air humidity transport equations can be written as follows:

$$\langle \rho \rangle (\vec{v} \cdot \nabla) \vec{v} = -\nabla p + \langle \mu \rangle \nabla^2 \vec{v} \quad (1)$$

$$(\vec{v} \cdot \nabla) T = \langle \alpha \rangle \nabla^2 T \quad (2)$$

$$(\vec{v} \cdot \nabla) C = \langle D \rangle_{\text{LiBr-H}_2\text{O}(l)} \nabla^2 C \quad (3)$$

$$(\vec{v} \cdot \nabla) \omega = \langle D \rangle_{\text{air-H}_2\text{O}(v)} \nabla^2 \omega \quad (4)$$

where v , p , T , C , and ω are the mixture velocity, pressure, temperature, liquid-desiccant concentration, and air humidity ratio, respectively. Also, $\langle \rho \rangle$ is the mixture density, $\langle \mu \rangle$ is the mixture dynamic viscosity, and $\langle \alpha \rangle$ is the mixture thermal diffusivity. The binary mass diffusion coefficients, $\langle D \rangle$, for the LiBr-water liquid and air-water vapor mixtures were considered as 1.3×10^{-9} and 2.2×10^{-5} , respectively.

In the second step, the Dusty-Gas model (Mason et al., 1926) was used to simulate the vapor flux through the membrane since the flow is in the transitional or free molecular flow regime. The physics of the Dusty-Gas model has been extensively discussed in our previous publications (Mortazavi et al., 2015; S Bigham et al., 2014; S Bigham et al., 2014). The vapor mass flux through the porous membrane (i.e., dehumidification rate) can be calculated from (S Bigham et al., 2014):

$$J = \kappa_m [P_v(T_{int}, \omega_{int}) - P_{s,w}(T_{int}, C_{int})] \quad (5)$$

where κ_m is the membrane permeability, P_v is the water vapor partial pressure of the air stream at the desiccant-air interface, T_{int} is the interface temperature, ω_{int} is the interface air humidity ratio, $P_{s,w}$ is the water vapor pressure of the LiBr solution at the interface, and C_{int} is the interface LiBr concentration. The membrane permeability or mass transfer coefficient is described by (S Bigham et al., 2014):

$$\kappa_m = -\frac{M}{\delta_m} \left(\frac{4\epsilon r}{3\tau} \sqrt{2/(\pi MRT)} + \frac{\epsilon r^2}{8\tau} \frac{p}{RT\mu} \right) \quad (6)$$

where M , δ_m , ϵ , r , τ , R , μ , and p are the molecular weight, membrane thickness, membrane porosity, membrane pore size, membrane tortuosity, gas constant, the water vapor dynamic viscosity, and total pressure, respectively.

Since the two phases are in a thermodynamic equilibrium state at the desiccant-air interface, the energy balance equation at the desiccant-air interface can be written as follows:

$$k_{air} \left(\frac{\partial T}{\partial n} \right)_{air} + \rho_{air} \langle D \rangle_{air-H_2O(v)} \frac{\partial \omega}{\partial n} h_{fg} = k_{LiBr} \left(\frac{\partial T}{\partial n} \right)_{LiBr} \quad (7)$$

where k_{air} , ρ_{air} , h_{fg} , and k_{LiBr} are the air thermal conductivity, air density, latent heat of vaporization, and LiBr thermal conductivity, respectively. As evident, the heat of absorption released at the interface is transferred to both air and desiccant media.

The mass balance equation at the desiccant-air interface can be written as follows:

$$\rho_{air} \langle D \rangle_{air-H_2O(v)} \frac{\partial \omega}{\partial n} = \rho_{LiBr} \langle D \rangle_{LiBr-H_2O(l)} \frac{\partial C}{\partial n} \quad (8)$$

where ρ_{LiBr} is the LiBr density. The dehumidification rate can be also estimated as follows:

$$J = \rho_{LiBr} \langle D \rangle_{LiBr-H_2O(l)} \frac{\partial C}{\partial n} \quad (9)$$

Therefore, the unknown parameters at the desiccant-air interface (i.e., T_{int} , C_{int} , ω_{int} , and J) are obtained by solving Eqs. (5) and 7-9 simultaneously.

At the membrane surface, no-slip boundary condition is assumed for the momentum transport equations of the desiccant and air phases. The desiccant and air temperatures, desiccant concentration, and air humidity ratio are specified at the inlet boundaries, while a zero gradient boundary condition is applied for the temperature, concentration, and humidity ratio at the solution and air outlet boundaries. Also, adiabatic, and symmetric boundary conditions are used for the left solid wall and the right air-side flow domain, respectively (cf. Fig. 1).

In addition, latent effectiveness (η_{latent}) and total effectiveness (η_{total}) are defined to evaluate performance of the dehumidification process. The latent effectiveness is defined as the ratio of actual air humidity ratio change to maximum possible humidity ratio difference in the system. Also, the total effectiveness is defined as the ratio of actual air enthalpy change to maximum possible enthalpy difference between air and solution in the system.

$$\eta_{latent} = \frac{\omega_{air,in} - \omega_{air,out}}{\omega_{air,in} - \omega_{air,eq}} \times 100 \quad (10)$$

$$\eta_{total} = \frac{h_{air,in} - h_{air,out}}{h_{air,in} - h_{air,eq}} \times 100 \quad (11)$$

where $\omega_{air,in}$, $\omega_{air,out}$, and $\omega_{air,eq}$ are the air inlet humidity ratio, the air outlet humidity ratio, and the air humidity ratio at equilibrium

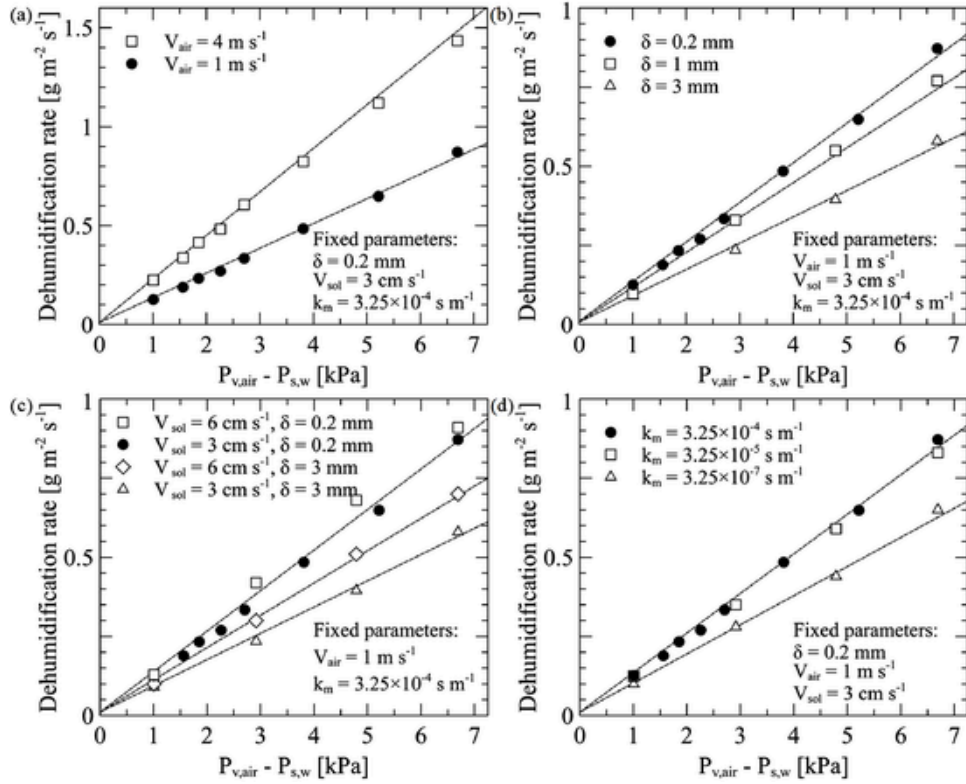


Fig. 8. Variations of moisture removal rate versus water vapor pressure potential at (a) air flow velocities of 1 and 4 m s⁻¹, (b) solution film thicknesses of 0.2, 1, and 3 mm, (c) solution flow velocities of 3 and 6 cm s⁻¹ and solution film thickness of 0.2 and 3 mm, and (d) membrane permeabilities of 3.25 × 10⁻⁴, 3.25 × 10⁻⁵, and 3.25 × 10⁻⁷ s m⁻¹.

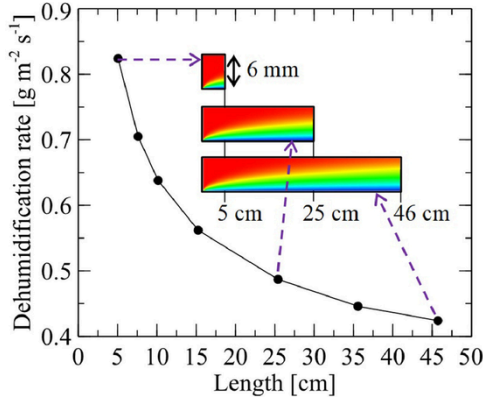


Fig. 9. Variations of moisture removal rate versus liquid desiccant absorber length at an inlet air flow velocity of 4 m s⁻¹.

state. In addition, $h_{air,in}$, $h_{air,out}$, $h_{air,eq}$ are the air inlet enthalpy, the air outlet enthalpy, and the air enthalpy at equilibrium state. The equilibrium is a state at which the water vapor partial pressure of air is equal to the water vapor pressure at the air-desiccant interface.

A finite-volume based solver, ANSYS Fluent, was employed to solve the above equations. The desiccant/air temperature and concentration boundary conditions at the membrane interphase (Eqs. (5)–(9)) were implemented via a user-defined function (UDF) written in a C code. In the UDF, first, computational cells adjacent to the desiccant-air interface are detected. Then, the concentration and temperature gradients normal to the interface for both liquid and air phases are calculated. Finally, using Eqs. (5)–(9), desiccant and air temperatures, desiccant concentration, and air humidity ratio are updated. A double-precision floating-point solver was employed to solve the governing equations with a convergence criterion of 10⁻¹² for residuals. Fig. 1 shows a

schematic of the liquid-desiccant dehumidifier model. As shown, the dehumidifier module has a cross flow configuration in which the desiccant solution and the humid air steam flow in vertical and horizontal directions, respectively. The flow is considered laminar. The two flow streams are separated by a porous superhydrophobic membrane. The nominal thicknesses of the desiccant and air flow channels are 200 μm and 3 mm, respectively. Table 1 provides a list of input parameters to the numerical model.

A grid independence study was performed to ensure independency of the computational results from the grid size. Structured hexahedron meshes were employed for both liquid-desiccant and air domains. A boundary layer mesh was also adopted to resolve high temperature and species gradients normal to the desiccant-air interface. Fig. 2a shows dehumidification rate at different numbers of computational elements. The simulations were conducted for the nominal conditions listed in Table 1. As shown, the dehumidification rate converges into a fixed value as the number of computational elements increases. Upon the grid independence study, a minimum element size of 3 micrometers resulting in more than 2.4 million computational elements was chosen. The accuracy of the numerical model was validated against experimental results of a cross-flow membrane-based liquid-desiccant air dehumidifier reported by Chen et al. (Chen et al., 2017). Fig. 2b showing the effect of water vapor partial pressure of the air on the absorption rate compares simulation results of the present study against experimental results of Chen et al. (Chen et al., 2017). As evident, the numerical model well predicts the experimental data with a maximum deviation of less than 11%.

3. Results and discussion

Fig. 3a illustrates the LiBr concentration contours in a vertical mid-plane within the desiccant flow channel. A scale factor of 200 in the direction normal to the interface is used to show the entire flow do-

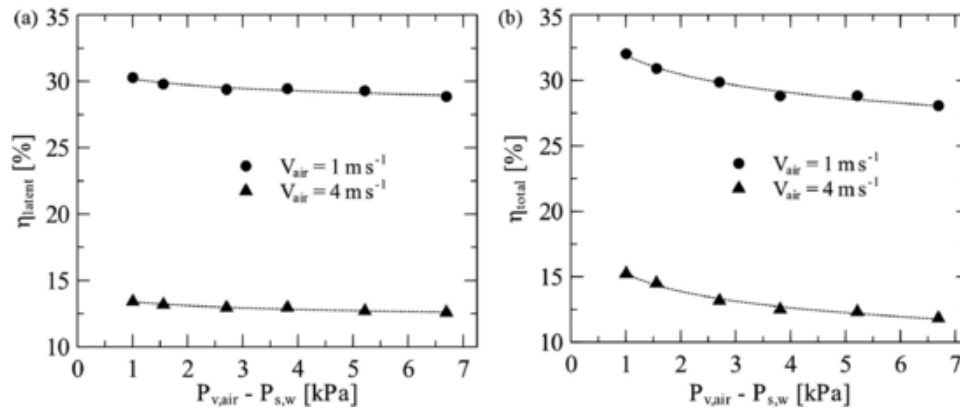


Fig. 10. Variations of the (a) latent, and (b) total effectiveness versus water vapor pressure potential at two air flow velocities of 1 and 4 m s^{-1} .

main. A strong LiBr solution with a concentration of 55% colored in red enters the desiccant channel. The LiBr solution has a high affinity to capture water vapor through a vapor-permeable membrane at the desiccant-air interface. As LiBr solution absorbs the airborne humidity, its concentration decreases to establish a local thermodynamic equilibrium at each interfacial cell. This results in formation and growth of a mass boundary layer at the desiccant-air interface. Being a resistance to mass transfer process, the desiccant mass boundary layer prevents the strong LiBr solution to reach the desiccant-air interphase and absorb humidity more effectively.

Additionally, Fig. 3a indicates that most of the strong LiBr solution does not contribute to the absorption process. This unnecessarily increased the LiBr mass flow rate flowing through the dehumidifier module. A higher desiccant mass flow rate could increase required pumping power of the LiBr solution as well as thermal energy needed for a subsequent desorption process. For a given length of the absorber module, the LiBr solution could be effectively involved in the absorption process if thickness of the desiccant film decreases.

Fig. 4 shows variations of the average LiBr concentration along the desiccant flow channel. As shown, the LiBr concentration rapidly declines at the solution inlet. This can be attributed to the mass boundary layer thickness which is thin at the solution inlet, thereby leading to a high moisture absorption rate. The bulk LiBr concentration, then, steadily decreases as the thickness of the mass boundary layer grows along the flow direction.

Fig. 3b depicts the LiBr temperature contours in a vertical mid-plane within the desiccant flow channel. Fig. 4 shows variations of the corresponding bulk LiBr temperature along the desiccant flow channel. The temperature of the LiBr solution at the inlet is 30 °C. As shown, the bulk LiBr temperature steadily increases along the desiccant flow direction. This is partially attributed to heat of the absorption process released at the desiccant-air interface, which increases the solution temperature along the flow direction. The LiBr temperature is also affected by the air flow stream entering at a higher temperature of 35 °C.

Fig. 5a represents the air relative humidity (Φ) distribution contours in a horizontal mid-plane within the air flow channel. Fig. 6 shows corresponding variations in the bulk air relative humidity along the air flow channel. The relative humidity of the air flow stream at the inlet is 80%. The LiBr solution present at the desiccant-air interface captures the air humidity, resulting in a relatively dry air manifested by the blue color of the air relative humidity counter at the interface. The air remains dry at a relative humidity of approximately 18% along the desiccant-air interface, signifying a superior performance functionality of the LiBr desiccant. This indicates that the dehumidification process of an open-air stream is mainly limited by the interface boundary layer grown in the air flow domain rather than that of the desiccant flow domain. In other words, to effectively increase the dehumidification rate, attempts should be largely focused on reducing thickness of

the moisture boundary layer present in the air-side flow domain. This could be accomplished, for instance, by enhanced mixing using textured surfaces or a smaller air gap channel. Additionally, the relative humidity contours shown in Fig. 5a indicates the current air flow channel needs to be either longer and/or thinner to ensure involvement of all air particles in the dehumidification process at the simulated air flow condition.

Fig. 5b illustrates contours of the air temperature distribution in a horizontal mid-plane within the air flow channel. Corresponding variations in the bulk air temperature along the air flow channel is shown in Fig. 6. The air temperature at the inlet is 35 °C. As shown, the air temperature initially increases at the desiccant-air interface. This is because of a strong dehumidification rate at the inlet of the air flow channel where the moisture boundary layer is thin and the water vapor pressure potential is considerably high. The air temperature, however, then decreases along the air flow channel. This is attributed to the lower temperature of the LiBr solution stream, which cools down the air flow stream.

Fig. 7 shows variations of moisture removal rate versus air relative humidity at different air inlet temperatures and two inlet air flow velocities of 1 and 4 m s^{-1} . As shown, the moisture absorption rate increases at higher air relative humidity and temperatures (i.e., at higher air humidity ratios). This is attributed to the water vapor partial pressure of the air stream, which increases at higher air humidity ratios. The water vapor pressure potential (i.e., the water vapor partial pressure difference between the air and solution sides) drives the dehumidification process. Additionally, the dehumidification rate increases at higher air inlet velocities. This is because the mass transport boundary layer shrinks at higher air velocities, thereby increasing the moisture removal rate.

Fig. 8 shows variations of moisture removal rate with respect to water vapor pressure potential at two different air flow velocities of 1 and 4 m s^{-1} , solution flow velocities of 3 and 6 cm s^{-1} , membrane permeabilities of 3.25×10^{-4} , 3.25×10^{-5} , and $3.25 \times 10^{-7} \text{ s m}^{-1}$, and solution film thicknesses of 0.2, 1, and 3 mm. The high, medium, and low permeability values selected approximately represent membrane pore diameters of 5, 1, and 0.02 μm , respectively (Isfahani et al., 2013). As evident, the moisture removal rate linearly increases with the water vapor pressure potential (i.e., $J = \alpha \Delta P$) for a given transport condition (i.e., fixed air and solution flow conditions and membrane characteristics). The water vapor pressure potential represents the thermodynamic state of the dehumidification process. The slope of the dehumidification curve versus water vapor pressure potential (i.e., α) depends on hydraulic transport characteristics of the membrane, air stream, and desiccant solution.

Fig. 8a indicates that the dehumidification rate increases at higher air flow velocities. For instance, at a water vapor pressure potential of 5 kPa, the dehumidification rate boosts from 0.65 to 1.1 $\text{g m}^{-2} \text{ s}^{-1}$,

a 70% improvement in the moisture removal rate when the air velocity increases from 1 to 4 m s⁻¹. This is mainly attributed to the thickness of the moisture boundary layer, which shrinks at higher air flow velocities. This consequently reduces mass transfer resistance within the air flow stream, thereby increasing the dehumidification rate. Fig. 8b shows the dehumidification rate versus water vapor pressure potential at three solution film thicknesses of 0.2, 1, and 3 mm. As evident, the dehumidification rate decreases with the solution film thickness. This is because the solution-side mass boundary layer grows in thickness at higher film thicknesses, thereby decreasing the moisture removal rate. Fig. 8c shows that the dehumidification rate is not affected by the solution velocity when the solution film thickness is thin (e.g., 0.2 mm). For example, at a solution film thickness of 0.2 mm, the dehumidification rate remains almost constant when the LiBr velocity increases from 3 to 6 cm s⁻¹. However, at higher solution film thicknesses, the dehumidification rate moderately increases with the solution velocity. The effect of membrane permeability on the dehumidification rate is shown in Fig. 8d. As evident, the dehumidification rate remains almost constant when the membrane permeability varies from 3.25 × 10⁻⁴ to 3.25 × 10⁻⁵ s m⁻¹ which is a typical permeability range for commonly used porous superhydrophobic membranes. However, the dehumidification rate substantially decreases when the membrane permeability significantly decreases from 3.25 × 10⁻⁵ to 3.25 × 10⁻⁷ s m⁻¹. Therefore, it can be concluded that the air dehumidification process is mainly limited by the air-side transport physics for thin liquid-desiccant films and commonly used porous superhydrophobic membranes. Additionally, the air dehumidification process is limited by transport physics of both air and desiccant sides for thick liquid desiccant films and commonly used superhydrophobic membranes.

Fig. 9 depicts the dehumidification rate at different lengths of the liquid-desiccant absorber module. As shown, the moisture removal rate decreases as the absorber length increases. This is attributed to the thickness of the air relative humidity boundary layer, which grows along the absorber length. Therefore, a longer dehumidifier has a thicker mass boundary layer, thereby reducing the average moisture extraction rate. The simulation results indicate that the dehumidification rate decreases by 49% when the absorber length (length-to-height channel ratio) increases from 5 cm (8.3) to 46 cm (76.7).

Fig. 10 shows performance of the dehumidification process evaluated by the latent and total effectiveness at different water vapor pressure potentials and two air flow velocities of 1 and 4 m s⁻¹. As shown, both latent and total effectiveness decrease at higher air flow velocities. This is attributed to the actual air humidity ratio and enthalpy changes, which decrease at higher air flow rates. In addition, the latent and total effectiveness slightly decrease at higher water vapor pressure potentials. In other words, the membrane-based dehumidification process is more effective at lower water vapor pressure potentials.

4. Conclusion

Detailed 3D, two-phase (i.e., liquid and gas phases), multi-species CFD simulations were conducted to comprehensively analyze performance of a membrane-based liquid-desiccant dehumidification system. The simulations were conducted over a wide range of desiccant thermo-hydraulic and ambient air conditions representing peak climates of some largest cities in the world. The results were both extensive and specific to guide design of future SSLC systems potentially utilizing membrane-based dehumidifier modules.

Decoupling the roles of the thermodynamic and hydraulic effects in the membrane-based liquid-desiccant dehumidification process, the simulations revealed the underlying mechanisms of the dehumidification process including the rate-limiting step. It was found that the dehumidification rate is a linear function of the water vapor pressure potential ($J = \alpha \Delta P$) summarizing thermodynamic state of the system. Also,

the slope of the dehumidification curve (i.e., α) depends on hydraulic transport characteristics of the membrane, air stream, and desiccant solution. It was found that the moisture removal rate of a membrane-based air dehumidifier is mainly limited by the air-side transport physics for thin liquid-desiccant films and commonly used porous superhydrophobic membranes. A maximum dehumidification rate of 1.4 g m⁻² s⁻¹ at an air temperature of 40 °C, relative humidity of 100% and velocity of 4 m s⁻¹ was observed. The total energy effectiveness of the dehumidification process varies from 13 to 34% depending on ambient and system conditions. In addition, the average dehumidification rate decreases as the length of the absorber module increases mainly due to the moisture boundary layer thickness growth.

Declaration of Competing Interest

The authors declare that they have no known competing financial interests or personal relationships that could have appeared to influence the work reported in this paper.

Acknowledgments

This study was sponsored by the US Department of Energy's Office of Energy Efficiency and Renewable Energy (EERE) under the Building Technology Office Award Number DE-EE0008685. The authors would like to acknowledge Mr. Antonio Bouza and Mr. Mohammed Khan, Technology Managers, and Mr. Michael Geocarri and Mr. Andrew Kobusch, Project Engineers, HVAC, Water Heating, and Appliance sub-program, Building Technologies Office, US Department of Energy.

References

- Afrasiabian, E., Iliiev, O., Shklyar, I., Prill, T., Isetti, C., Lazzari, S., 2019. 3D-CFD analysis of the effect of cooling via minitubes on the performance of a three-fluid combined membrane contactor. *Int J Low-Carbon Technol* 14, 400–409. <https://doi.org/10.1093/ijlct/ctz033>.
- Asfand, F., Bourouis, M., 2015. A review of membrane contactors applied in absorption refrigeration systems. *Renew Sustain Energy Rev* 45, 173–191.
- Bahreghmand, H., Bahrami, M., 2019. An analytical design tool for sorber bed heat exchangers of sorption cooling systems. *Int. J. Refrig.* 100, 368–379. <https://doi.org/10.1016/j.ijrefrig.2019.02.003>.
- Bai, H., Zhu, J., Chen, X., Chu, J., Cui, Y., Yan, Y., 2020. Steady-state performance evaluation and energy assessment of a complete membrane-based liquid desiccant dehumidification system. *Appl. Energy* 258, 114082. <https://doi.org/10.1016/j.apenergy.2019.114082>.
- Bai, H., Zhu, J., Chen, Z., Ma, L., Wang, R., Li, T., 2017. Performance testing of a cross-flow membrane-based liquid desiccant dehumidification system. *Appl. Therm. Eng.* 119, 119–131. <https://doi.org/10.1016/j.applthermaleng.2017.03.058>.
- Bigham, S., Nasr Isfahani, R., Moghaddam, S., 2014b. Direct molecular diffusion and micro-mixing for rapid dewatering of libr solution. *Appl. Therm. Eng.* 64, 371–375.
- Bigham, S., Yu, D., Chugh, D., Moghaddam, S., 2014a. Moving beyond the limits of mass transport in liquid absorbent microfilms through the implementation of surface-induced vortices. *Energy* 65, 621–630.
- Cabeza, L.F., Solé, A., Barreneche, C., 2017. Review on sorption materials and technologies for heat pumps and thermal energy storage. *Renew Energy* 110, 3–39. <https://doi.org/10.1016/j.renene.2016.09.059>.
- Chen, Z., Zhu, J., Bai, H., Yan, Y., Zhang, L., 2017. Experimental study of a membrane-based dehumidification cooling system. *Appl. Therm. Eng.* 115, 1315–1321. <https://doi.org/10.1016/j.applthermaleng.2016.10.153>.
- Cheng, X., Rong, Y., Zhou, X., Gu, C., Zhi, X., Qiu, L., et al., 2020. Performance analysis of a multistage internal circulation liquid desiccant dehumidifier. *Appl. Therm. Eng.* 172, 115163. <https://doi.org/10.1016/j.applthermaleng.2020.115163>.
- Cho, H.-J., Cheon, S.-Y., Jeong, J.-W., 2019. Experimental analysis of dehumidification performance of counter and cross-flow liquid desiccant dehumidifiers. *Appl. Therm. Eng.* 150, 210–223. <https://doi.org/10.1016/j.applthermaleng.2019.01.006>.
- Chu, J., Zhu, J., Bai, H., Cui, Y., 2019. Experimental study of a membrane-based liquid desiccant dehumidifier based on internal air temperature variation. *Appl. Therm. Eng.* 159, 113936. <https://doi.org/10.1016/j.applthermaleng.2019.113936>.
- Comino, F., Táboas, F., Peci, F., Ruiz de Adana, M., 2020. Detailed experimental analysis of the energy performance of a desiccant wheel activated at low temperature. *Appl. Therm. Eng.* 178, 115580. <https://doi.org/10.1016/j.applthermaleng.2020.115580>.
- Das, R.S., Jain, S., 2015. Performance characteristics of cross-flow membrane contactors for liquid desiccant systems. *Appl. Energy* 141, 1–11. <https://doi.org/10.1016/j.apenergy.2014.12.014>.
- Ge, T.S., Li, Y., Wang, R.Z., Dai, Y.J., 2009. Experimental study on a two-stage rotary desiccant cooling system. *Int. J. Refrig.* 32, 498–508. <https://doi.org/10.1016/j.ijrefrig.2008.07.001>.

- Goldsworthy, M., White, S.D., 2012. Limiting performance mechanisms in desiccant wheel dehumidification. *Appl. Therm. Eng.* 44, 21–28. <https://doi.org/10.1016/j.applthermaleng.2012.03.046>.
- Higashi, T., Yamaguchi, M., Nakagawa, N., Dang, C., Hihara, E., 2018. Gravimetric method for sorption performance measurement of desiccant wheel and desiccant coated heat exchanger. *Appl. Therm. Eng.* 144, 639–646. <https://doi.org/10.1016/j.applthermaleng.2018.05.079>.
- Huang, S.-M., Yang, M., Hong, Y., Ye, W.-., 2018. Performance correlations of an adjacently internally-cooled membrane contactor applied for liquid desiccant air dehumidification. *Appl. Therm. Eng.* 129, 1660–1669. <https://doi.org/10.1016/j.applthermaleng.2017.10.154>.
- Huang, S.-M., Yang, M., Yang, X., 2014. Performance analysis of a quasi-counter flow parallel-plate membrane contactor used for liquid desiccant air dehumidification. *Appl. Therm. Eng.* 63, 323–332. <https://doi.org/10.1016/j.applthermaleng.2013.11.027>.
- Huang, S.-M., Zhang, L.-Z., Tang, K., Pei, L.-X., 2012b. Turbulent heat and mass transfer across a hollow fiber membrane tube bank in liquid desiccant air dehumidification. *J. Heat Transfer* 134. <https://doi.org/10.1115/1.4006208>.
- Huang, S.-M., Zhang, L.-Z., Yang, M., 2013. Conjugate heat and mass transfer in membrane parallel-plates ducts for liquid desiccant air dehumidification: effects of the developing entrances. *J. Memb. Sci.* 437, 82–89. <https://doi.org/10.1016/j.memsci.2013.02.048>.
- Huang, S.M., Zhang, L.Z., Tang, K., Pei, L.X., 2012a. Fluid flow and heat mass transfer in membrane parallel-plates channels used for liquid desiccant air dehumidification. *Int. J. Heat Mass Transf.* 55, 2571–2580. <https://doi.org/10.1016/j.ijheatmasstransfer.2012.01.003>.
- IEA, The future of cooling - Opportunities for energy-efficient air conditioning. International Energy Agency; 2018. <https://doi.org/10.1787/9789264301993-en>.
- Isfahani, R.N., Sampath, K., Moghaddam, S., 2013. Nanofibrous membrane-based absorption refrigeration system. *Int. J. Refrig.* 36, 2297–2307. <https://doi.org/10.1016/j.ijrefrig.2013.07.019>.
- Jafarian, H., Sayyaadi, H., Torabi, F., 2019. Numerical modeling and comparative study of different membrane-based liquid desiccant dehumidifiers. *Energy Convers. Manag.* 184, 735–747. <https://doi.org/10.1016/j.enconman.2019.01.099>.
- Kozubal E., Woods J., Burch J., Boranian A., Merrigan T. Desiccant enhanced evaporative air-conditioning (DEVap): evaluation of a new concept in ultra efficient air conditioning. Tech Report, NREL/TP-5500-49722 2011;303:275–3000. <https://doi.org/10.2172/1004010>.
- Lee, H., Lin, X., Hwang, Y., Radermacher, R., 2016. Performance investigation on solid desiccant assisted mobile air conditioning system. *Appl. Therm. Eng.* 103, 1370–1380. <https://doi.org/10.1016/j.applthermaleng.2016.05.053>.
- Lin, J., Huang, S.M., Wang, R., Jon Chua, K., 2019. On the in-depth scaling and dimensional analysis of a cross-flow membrane liquid desiccant dehumidifier. *Appl. Energy* 250, 786–800. <https://doi.org/10.1016/j.apenergy.2019.05.074>.
- Ling, J., Kuwabara, O., Hwang, Y., Radermacher, R., 2013. Enhancement options for separate sensible and latent cooling air-conditioning systems. *Int. J. Refrig.* 36, 45–57. <https://doi.org/10.1016/j.ijrefrig.2012.09.003>.
- Liu, X., Qu, M., Liu, X., Wang, L., 2019. Membrane-based liquid desiccant air dehumidification: a comprehensive review on materials, components, systems and performances. *Renew. Sustain. Energy Rev.* 110, 444–466. <https://doi.org/10.1016/j.rser.2019.04.018>.
- Luo, Y., Chen, Y., Yang, H., Wang, Y., 2017. Study on an internally-cooled liquid desiccant dehumidifier with CFD model. *Appl. Energy* 194, 399–409. <https://doi.org/10.1016/j.apenergy.2016.05.133>.
- Mason, E.A., Malinauskas, A.P., Mason, E., . . . A., 1926. *Gas Transport in Porous Media: the Dusty-Gas Model*. Elsevier Scientific Pub., New York.
- Misha, S., Mat, S., Ruslan, M.H., Sopian, K., 2012. Review of solid/liquid desiccant in the drying applications and its regeneration methods. *Renew. Sustain. Energy Rev.* 16, 4686–4707. <https://doi.org/10.1016/j.rser.2012.04.041>.
- Mortazavi, M., Nasr Isfahani, R., Bigham, S., Moghaddam, S., 2015. Absorption characteristics of falling film LiBr (lithium bromide) solution over a finned structure. *Energy* 87, 270–278. <https://doi.org/10.1016/j.energy.2015.04.074>.
- Narayanan, R., Saman, W.Y., White, S.D., 2013. A non-adiabatic desiccant wheel: modeling and experimental validation. *Appl. Therm. Eng.* 61, 178–185. <https://doi.org/10.1016/j.applthermaleng.2013.07.007>.
- Nasr Isfahani, R., Fazeli, A., Bigham, S., Moghaddam, S., 2014. Physics of lithium bromide (LiBr) solution dehumidification through vapor venting membranes. *Int. J. Multiph. Flow* 58, 27–38. <https://doi.org/10.1016/j.ijmultiphaseflow.2013.08.005>.
- O'Connor, D., Calautit, J.K., Hughes, B.R., 2016. A novel design of a desiccant rotary wheel for passive ventilation applications. *Appl. Energy* 179, 99–109. <https://doi.org/10.1016/j.apenergy.2016.06.029>.
- Pandelidis, D., Pacak, A., Cichoń, A., Drag, P., Worek, W., Cetin, S., 2020. Numerical and experimental analysis of precooled desiccant system. *Appl. Therm. Eng.* 181, 115929. <https://doi.org/10.1016/j.applthermaleng.2020.115929>.
- Park, J.Y., Kim, B.J., Yoon, S.Y., Byon, Y.S., Jeong, J.W., 2019. Experimental analysis of dehumidification performance of an evaporative cooling-assisted internally cooled liquid desiccant dehumidifier. *Appl. Energy* 235, 177–185. <https://doi.org/10.1016/j.apenergy.2018.10.101>.
- Raisul Islam, M., Wijesundera, N., Ho, J., 2003. Performance study of a falling-film absorber with a film-inverting configuration. *Int. J. Refrig.* 26, 909–917. [https://doi.org/10.1016/S0140-7007\(03\)00078-1](https://doi.org/10.1016/S0140-7007(03)00078-1).
- Rashidzadeh, M., Pourmahmoud, N., Simonson, C.J., 2019. 3D computational fluid dynamics simulation of a 3-fluid liquid-to-air membrane energy exchanger (LAMEE). *Appl. Therm. Eng.* 153, 501–512. <https://doi.org/10.1016/j.applthermaleng.2019.03.010>.
- Ren, H., Ma, Z., Liu, J., Gong, X., Li, W., 2019. A review of heat and mass transfer improvement techniques for dehumidifiers and regenerators of liquid desiccant cooling systems. *Appl. Therm. Eng.* 162, 114271. <https://doi.org/10.1016/j.applthermaleng.2019.114271>.
- Restuccia, G., Freni, A., Russo, F., Vasta, S., 2005. Experimental investigation of a solid adsorption chiller based on a heat exchanger coated with hydrophobic zeolite. *Appl. Therm. Eng.* 25, 1419–1428. <https://doi.org/10.1016/j.applthermaleng.2004.09.012>.
- Shen, S., Cai, W., Wang, X., Wu, Q., Yon, H., 2016. Hybrid model for heat recovery heat pipe system in liquid desiccant dehumidification system. *Appl. Energy* 182, 383–393. <https://doi.org/10.1016/j.apenergy.2016.08.128>.
- Su, W., Li, W., Zhou, J., Zhang, X., 2018. Experimental investigation on a novel frost-free air source heat pump system combined with liquid desiccant dehumidification and closed-circuit regeneration. *Energy Convers. Manag.* 178, 13–25. <https://doi.org/10.1016/j.enconman.2018.09.085>.
- Tao, W., Yimo, L., Lin, L., 2019. A novel 3D simulation model for investigating liquid desiccant dehumidification performance based on CFD technology. *Appl. Energy* 240, 486–498. <https://doi.org/10.1016/j.apenergy.2019.02.068>.
- Tu, R., Hwang, Y., Cao, T., Hou, M., Xiao, H., 2018. Investigation of adsorption isotherms and rotational speeds for low temperature regeneration of desiccant wheel systems. *Int. J. Refrig.* 86, 495–509. <https://doi.org/10.1016/j.ijrefrig.2017.11.008>.
- Tu, R., Liu, X.H., Jiang, Y., 2014. Performance analysis of a two-stage desiccant cooling system. *Appl. Energy* 113, 1562–1574. <https://doi.org/10.1016/j.apenergy.2013.09.016>.
- Wen, T., Lu, L., 2019. A review of correlations and enhancement approaches for heat and mass transfer in liquid desiccant dehumidification system. *Appl. Energy* 239, 757–784. <https://doi.org/10.1016/j.apenergy.2019.01.245>.
- Woods, J., Kozubal, E., 2018. On the importance of the heat and mass transfer resistances in internally-cooled liquid desiccant dehumidifiers and regenerators. *Int. J. Heat Mass Transf.* 122, 324–340. <https://doi.org/10.1016/j.ijheatmasstransfer.2018.01.111>.
- Zhang, L.Z., Huang, S.M., Chi, J.H., Pei, L.X., 2012. Conjugate heat and mass transfer in a hollow fiber membrane module for liquid desiccant air dehumidification: a free surface model approach. *Int. J. Heat Mass Transf.* 55, 3789–3799. <https://doi.org/10.1016/j.ijheatmasstransfer.2012.03.034>.
- Zhang, L.-Z., 2011. An analytical solution to heat and mass transfer in hollow fiber membrane contactors for liquid desiccant air dehumidification. *J. Heat Transfer* 133. <https://doi.org/10.1115/1.4003900>.
- Zhou, X., Goldsworthy, M., Sproul, A., 2018. Performance investigation of an internally cooled desiccant wheel. *Appl. Energy* 224, 382–397. <https://doi.org/10.1016/j.apenergy.2018.05.011>.